

## Integration of improved meta-heuristic and machine learning for optimizing energy efficiency in additive manufacturing process

Baoyun Gao<sup>a</sup>, Shitong Peng<sup>a,\*</sup>, Tao Li<sup>b</sup>, Fengtao Wang<sup>a</sup>, Jianan Guo<sup>a,\*\*</sup>, Conghu Liu<sup>c</sup>, Hongchao Zhang<sup>d</sup>

<sup>a</sup> Department of Mechanical Engineering, Shantou University, Shantou, 515063, China

<sup>b</sup> School of Mechanical Engineering, Dalian University of Technology, Dalian, 116024, China

<sup>c</sup> School of Mechanical and Electronic Engineering, Suzhou University, Suzhou, 234000, China

<sup>d</sup> Department of Industrial, Manufacturing, & Systems Engineering, Texas Tech University, Lubbock, TX, 79409, United States

### ARTICLE INFO

Handling editor: Henrik Lund

**Keywords:**

Direct energy deposition  
Energy efficiency  
Geometrical appearance  
XGBoost  
Parameters optimization

### ABSTRACT

Additive manufacturing (AM) has been a vital element of smart manufacturing. The high energy intensity or environmental sustainability issue of AM, however, has posed a great challenge to the future massive application, particularly laser-based direct energy deposition (L-DED). This study aims to determine the optimal processing parameters for energy-saving without compromising the geometrical appearance. A quantification model for energy efficiency at the process level was established, with two energy efficiency indicators of AM process. Then, a meta-heuristic Mayfly algorithm, augmented with Bayesian technique and mutation strategies, was proposed to improve hyperparameters in a typical machine learning model (XGBoost). Based on the full factorial L-DED experiments, this study compared the improved XGBoost with four types of XGBoost derivatives via four algorithm evaluation metrics. Non-dominated sorting genetic algorithm II was adopted to optimize the processing parameters subject to the constraints of geometrical appearance. Results indicated that the proposed algorithm outperformed other XGBoost derivatives in terms of prediction accuracy and convergence rate. The energy efficiency could be improved by 76.35 J/g or 6.78 % on average while ensuring the geometry of the deposited layers. This study could help enhance energy-efficient additive manufacturing via proper processing parameters selection and facilitate the sustainability in AM domain.

### 1. Introduction

Smart manufacturing or industrial 4.0 relies heavily on additive manufacturing (AM) to decentralize production and manufacturing processes, enable mass customization, and strengthen supply networks [1]. AM builds, grows, or increases the mass of objects layer-upon-layer until they match the 3D digital model. These techniques were considered a “disruptive manufacturing technology” with a promising landscape to transform the manufacturing industry completely [2]. However, low energy efficiency and qualification issues have been regarded as the two significant barriers to broad and massive adoption of AM [3].

Although AM is featured with a lower by-to-fly-ratio, the electrical energy intensity of metal AM process is approximately 1–2 orders of magnitude higher compared with traditional subtractive manufacturing,

according to the statistical analysis of various AM technologies from process rate and power requirement perspectives [4]. Most energy performance studies of AM process were performed on machine level, i.e., evaluating the total energy consumption of subsystems including laser beam generator, controller, and cooling system under different operation modes. For example, comparative case studies [5,6] estimated the specific energy consumption (SEC) of additive and subtractive manufacturing by electricity consumption and deposition volume. Their studies indicated that the energy intensity of metal AM ( $1.53 \times 10^8$  J/kg) is particularly higher when fabricating less structurally complicated parts. The process level, however, is comparatively less studied and emphasizes more on the energy flow distribution. Previous studies have investigated the energy distributions on CO<sub>2</sub> laser cladding [7], Nd: YAG LENS process [8], and metal laser direct deposition [9]. According to these works, the energy ratio of melting metal materials ranged from

\* Corresponding author.

\*\* Corresponding author.

E-mail addresses: [shtpeng@stu.edu.cn](mailto:shtpeng@stu.edu.cn) (S. Peng), [jnguo@stu.edu.cn](mailto:jnguo@stu.edu.cn) (J. Guo).

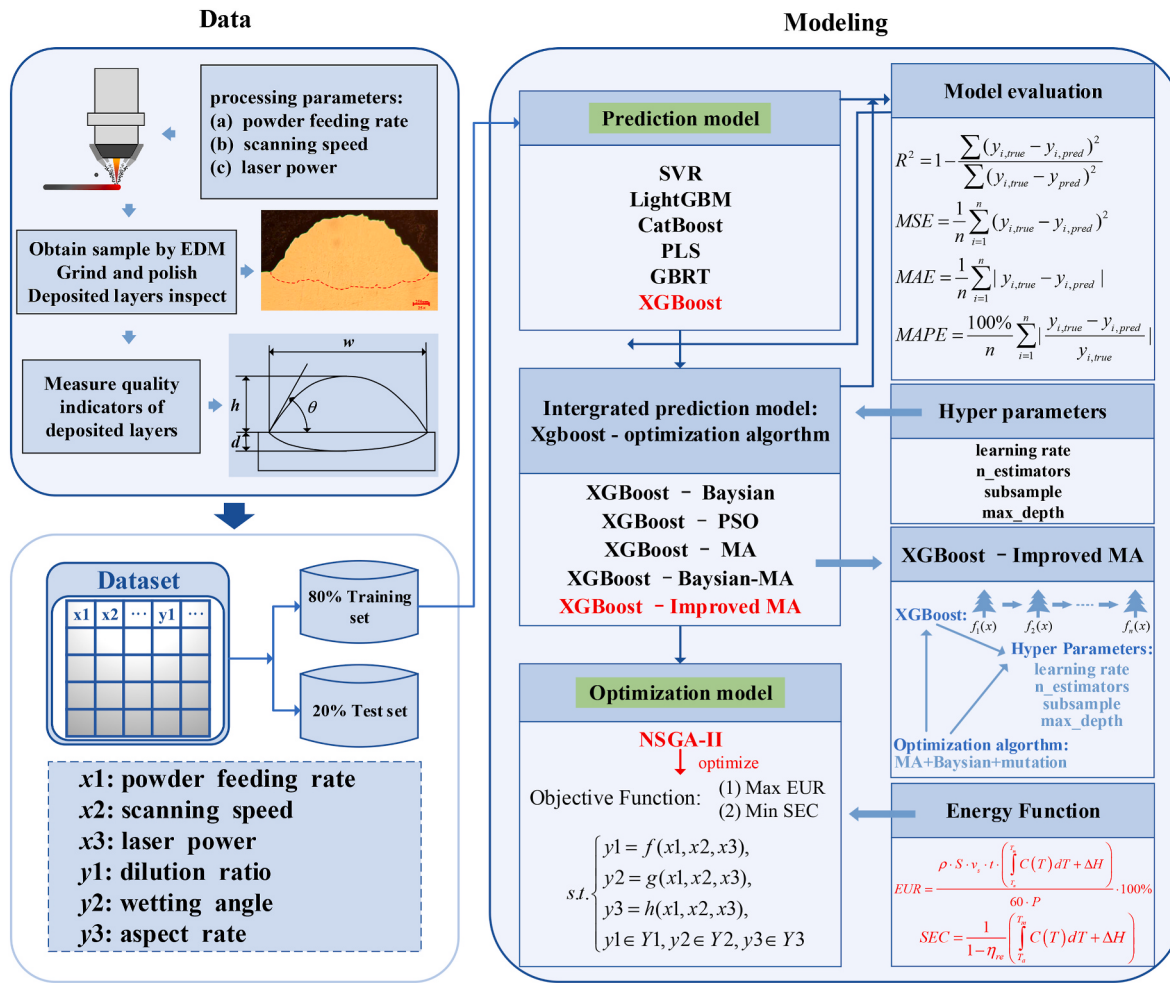


Fig. 1. Overview of prediction and optimization for L-DED.

10 % to 26 %, and the remainder of the energy was mainly reflected off by the molten pool and transferred away via heat. The low proportion of effective energy utilization implied the high potential improvement of energy intensity in the metal AM process.

Quality assurance is yet another challenge facing metal AM. Laser energy melts the metal powder on the prior deposited layer along with scanning direction, resulting in complex thermal cycles including heating, melting, cooling, and solidification processes. The re-heating and re-cooling processes generated highly non-uniform temperature fields, high-temperature gradients, and fast cooling rates. Mechanical anisotropy, residual stress, and molten-pool geometry are closely related to the energy inputs and thermal dissipation [10]. For example, the energy density (combining heat source power, scanning speed, powder feed rate, hatch spacing, etc.) largely determines the thermal history during processing. Insufficient energy density could increase the porosity and discontinuity in cladding layers [11], while higher energy density tends to obtain favorable metallurgy, microstructure, and mechanical properties [12]. Therefore, the energy efficiency and process quality of metal AM is two primary concerns.

The improvement of energy efficiency and quality performance in AM was popularly conducted from the perspective of processing parameters. There has been a body of studies optimizing the processing parameters towards the energy and quality in the metal AM process using heuristic algorithms, meta-heuristics algorithms, machine learning techniques, or statistical approaches. For example, Wu et al. developed an improved gene expression programming and non-dominated sorting genetic algorithm (NSGA-II) to optimize the total energy consumption of fiber laser welding [13]. Similarly, Osman et al.

analyzed the cost flows through the subcomponents of the plant and employed the NSGA-II to optimize the energy and exergy efficiencies [14]. Although prediction accuracy is a primary concern for mapping systematic input to output, most of the aforementioned studies merely obtain feasible results under limited data sets or even perform the optimization statistically and qualitatively. L-DED encompasses various factors that influence not only the energy efficiency of the production process but also the quality of the end product. Pedro et al. developed a machine learning model based on key process parameters affecting energy consumption in the plant, refining the fiberglass process for reduced energy usage [15]. Chung-Feng et al. optimized the crafted products by identifying the parameters with significant effects on quality characteristics [16]. The majority of studies tend to optimize solely based on either quality or energy usage, failing to sufficiently account for the interconnectedness between energy efficiency and the quality of the output. The optimization process primarily targets either quality or energy efficiency as singular objectives. However, the interconnected relationship between energy and quality factors is not sufficiently addressed. Laser energy, scanning speed, and powder feed rate are key parameters, to a large extent, determining the energy efficiency and mechanical properties of AM. Jinoop et al. focused on investigating the effects of process parameters on geometry and quality and fabricated defect-free L-DED products by optimizing process parameters [17]. How these processing parameters affect the energy absorption-dissipation process associated with powder, molten pool, and substrate still needs in-depth investigation for enhancing energy saving and quality performance.

Collectively, the pragmatic issues in typical metal AM process

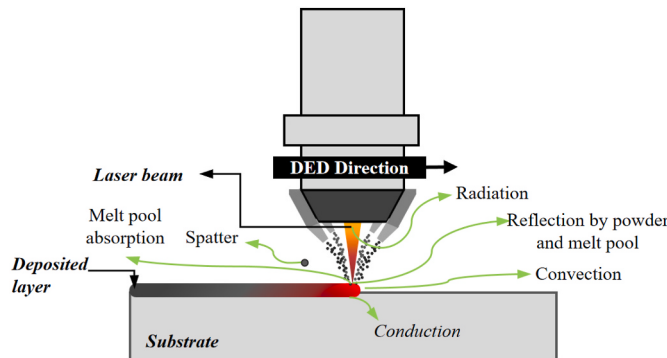


**Fig. 2.** Schematic of energy distribution in L-DED on process level.

regarding energy modeling and prediction rest on the following three aspects: (1) Randomly choosing a metamodel or statistical algorithm to conduct prediction can hardly get satisfactory accuracy, and the metamodels optimizing AM process remains to be improved for higher prediction accuracy; (2) Single objective optimization of AM process towards either energy or quality via processing parameters is presumably unfeasible in manufacturing practices; and (3) Influences of critical processing parameters on the coupling fabrication quality and energy consumption are still unclear.

To overcome the research gaps, the present study proposed a multi-objective prediction and optimization framework (Fig. 1) to systematically improve the overall performance and preliminarily explore the synergy mechanism of process energy and quality properties of parts. Of the typical forms of metal AM techniques, laser-based direct energy deposition (L-DED) is widely applied to the aircraft industry, nuclear power plants, and shipbuilding [18]. As shown in Fig. 1, in the L-DED experiment with Ti-10Mo titanium alloy powder, the SEC and energy utilization ratio (EUR) were selected as energy efficiency indicators at the process level and the geometrical appearance of deposited layers was adopted as quality performance criteria. With the data obtained from a full factorial experiment, the incorporation of Bayesian technique and mutation strategy-based meta-heuristics into the framework of extreme gradient boosting (XGBoost) was pursued for improving the hyperparameters of XGBoost. To validate the superior performance of the proposed algorithm, a comparative analysis was conducted against four XGBoost derivatives, employing four distinct algorithm evaluation metrics. Feature importance was analyzed to reveal the relative importance of each feature on the target variables. With the prediction models of energy efficiency and geometrical appearance, the Non-dominated Sorting Genetic Algorithm II (NSGA-II) was adopted to trade-off the energy efficiency indicators subject to the constraints of geometrical appearance requirements. The present study could help decrease the energy cost of AM manufacturers and facilitate environmental sustainability in the AM industry.

The rest of this article is organized as follows: Part 2 elaborated on the process energy characterization and efficiency indicators of L-DED. Part 3 described the detailed experimental setup and geometrical performance metrics. Part 4 presented algorithms for prediction and optimization, followed by the computational results in Part 5. Part 6 discussed sustainable and technical implications of energy efficiency optimization in the AM process. Part 7 concluded this study.

## 2. Process energy characterization and efficiency indicators

### 2.1. Process energy characterization

The total laser energy can be separated into two types, i.e., energy interacted with powder stream and transmitted energy [3], as shown in Fig. 2. The former included the energy absorbed by spatters, energy reflected by particles, and energy for heating powder. The latter

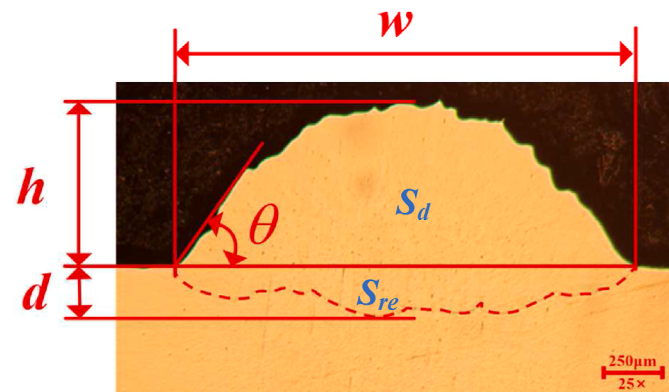


**Fig. 3.** A typical cross-section of the deposited layer under a microscope.

included the energy absorbed and reflected by the molten pool. Further, the energy absorbed by molten pool partially provided the enthalpy change required for melting and super-heating of molten pool, more specifically, the useful energy of AM process. Another part was dissipated via radiation, heat conduction, and convection. It should be noted that process parameters could influence the dynamic behaviors of energy absorption and dissipation.

According to the above descriptions, the process energy  $E$  regarding the deposited layer generation is comprised of the useful energy  $E_c$  and energy loss  $E_l$  as shown in Eq. (1).

$$E = E_c + E_l \quad (1)$$

The useful energy  $E_c$  is equivalent to the heat absorbed by the metal powder from ambient temperature to melting temperature. Eq. (2) expressed the  $E_c$  based on the enthalpy change of the molten metal material.

$$E_c = \rho \cdot S \cdot v_s \cdot t \cdot \left( \int_{T_a}^{T_m} C(T) dT + \Delta H \right) \quad (2)$$

where  $\rho$  is the density of substrate and powder materials in g/mm<sup>3</sup>,  $S$  is the cross-sectional area of the deposited layer in mm<sup>2</sup>,  $v_s$  is the scanning speed in mm/min,  $t$  is the processing time in s;  $T_a$  is the ambient temperature in K;  $T_m$  is the average temperature of the molten pool in K;  $C(T)$  is the specific heat capacity of metallic materials in J/(g·K); and  $\Delta H$  is the latent heat of fusion of metal materials in J/kg.

The energy loss  $E_l$  included energy reflected by the surface of molten pool ( $E_A$ ), energy reflected by the powder particles as they approach the molten pool ( $E_B$ ), energy lost by radiation ( $E_D$ ), energy lost by convection ( $E_E$ ), energy lost by conduction ( $E_F$ ), and energy absorbed by the powder particles spattered outside the molten pool ( $E_G$ ), as presented in Eq. (3):

$$E_l = E_A + E_B + E_D + E_E + E_F + E_G \quad (3)$$

According to the experimental results by Ref. [7], the radiated energy  $E_D$  can be estimated by:

$$E_D = \sigma T^4 A t \quad (4)$$

where  $\sigma$  denoted the Stefan-Boltzmann constant;  $T$  denoted the surface temperature of the melt in K;  $A$  denoted the area of the melt surface in mm<sup>2</sup>. Other terms in Eq. (3) can be estimated by thermodynamics and heat transfer principles or statistical analysis. Statistical data indicated that the  $E_D$ ,  $E_B$ ,  $E_A$ ,  $E_F$ ,  $E_G$ , and  $E_E$  account for 1 %, 9 %, 50.1 %, 30 %, 0.8 %, and 0.1 % of total process energy, respectively.

### 2.2. Process energy efficiency indicator

In the L-DED process, high energy laser beam melts not only metal

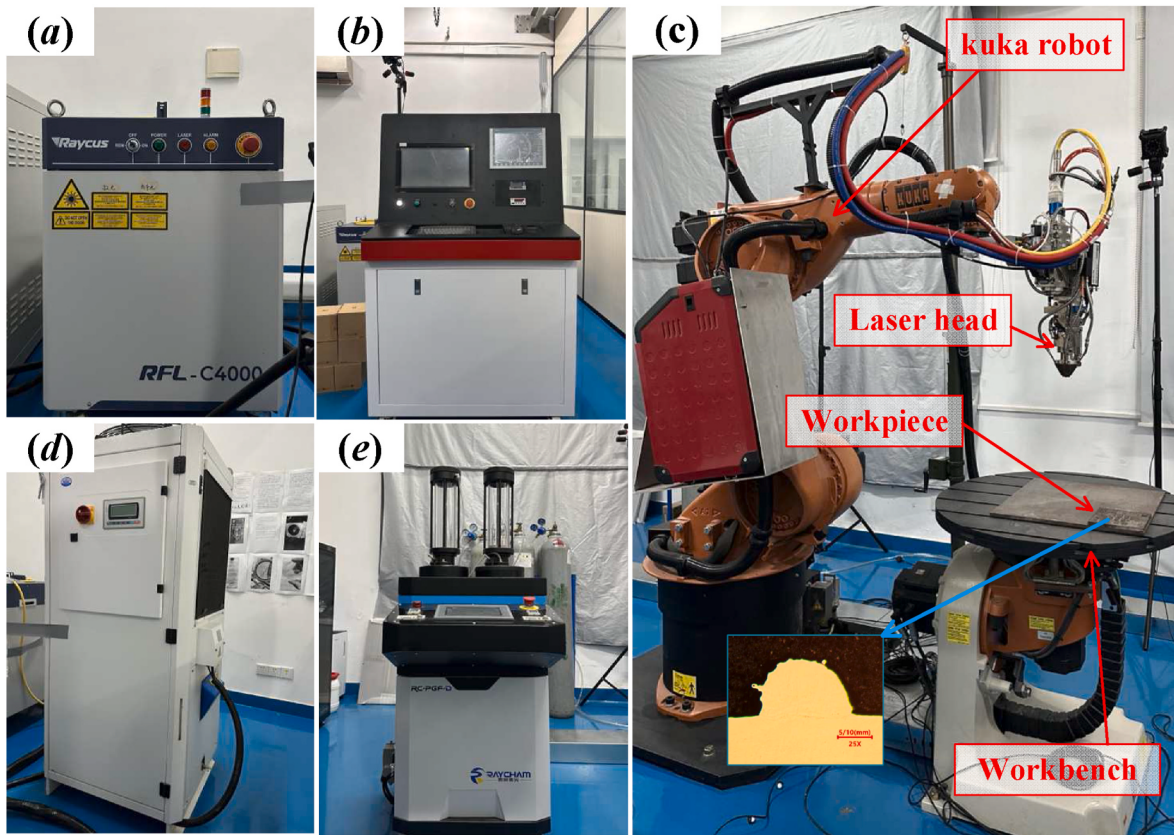


**Fig. 4.** Experimental platform of AM: (a) laser device; (b) control cabinet; (c) kinetic system; (d) water-cooling machine; and (e) powder feeder.

powder but also substrate or previously deposited layer to some extent and forms the remelting area, as shown in Fig. 3. The remelting area ensures that the newly deposited material is properly fused to the previously deposited material, creating a strong bond between the adjacent layers. The proportion of remelting area can be expressed by a dimensionless factor as presented below:

$$\eta_{re} = \frac{S_{re}}{S_{re} + S_d} \cdot 100\% \quad (5)$$

where  $\eta_{re}$  is the ratio of remelting area,  $S_d$  and  $S_{re}$  are the deposited area and remelted area in  $\text{mm}^2$ . The S in Eq. (2) equals the sum of  $S_d$  and  $S_{re}$ . Thus, the process energy efficiency indicator of EUR can be presented as follows:

$$EUR = \frac{E}{60 \cdot P} \cdot 100\% \quad (6)$$

where  $P$  denoted the laser power in W. EUR mainly characterizes the proportion of energy that creates the molten pool and heats deposited layers. It cannot illuminate the amounts of energy for building the deposited layers. Given the objective of achieving the desired parts, one expected to build more deposited volume for unit energy input. In this regard, it was desirable to increase the utilization of laser energy for forming the deposited layer while minimizing excessive fusion bonding. As a result, the SEC was introduced as an additional measure to assess energy efficiency at process level. Sec (J/g) is determined as follows:

$$SEC = \frac{E}{\rho \cdot S_d \cdot v_s} = \frac{\rho \cdot S \cdot v_s \cdot t \cdot \left( \int_{T_a}^{T_m} C(T) dT + \Delta H \right) + E_l}{\rho \cdot S_d \cdot v_s} \quad (7)$$

This equation can be further simplified as below:

**Table 1**  
Basic technical information of L-DED system.

Items	Parameters	Unit
Maximum output laser beam power	3000	W
Laser wavelength range	1075–1085	nm
Rated input voltage	3 × 380 - 3 × 575	V
Ambient temperature	5–45	°C
Repeated positioning accuracy	±0.05	mm
Filter wavelength	808 ± 20	mm
Maximum working radius of the robot	2033	mm
Flow rate of powder feeder	1–25	L/min
Operating frequency of the chiller	50	Hz

$$SEC = \frac{1}{1 - \eta_{re}} \left( \int_{T_a}^{T_m} C(T) dT + \Delta H \right) \quad (8)$$

As reflected in Eq. (7), greater  $S_d$  and smaller  $S_{re}$  implies better SEC for certain energy input. The bonding strength, however, might be deteriorated in such case. Thus, the process energy efficiency indicators could conflict with quality indicators.

### 3. Experimental procedure

#### 3.1. Experiment setup

Fig. 4 presented the experimental platform of the L-DED system, comprised of a laser device, control cabinet, kinetic system, water-cooling machine, and powder feeder. Table 1 provided the basic specifications of this system. Given this study concerns the energy consumption at process level rather than machine level, the power analyzer is not required in the experiment although this device is commonly used

**Table 2**

Chemical composition of Ti–10Mo titanium alloy powder (wt %).

Materials	Ti	Mo	C	N	O	S	Fe
Powder	Bal	10.39	0.05	0.01	0.13	0.08	0.01

in the investigation of the energy efficiency of manufacturing equipment [19–21]. Dong et al. analyzed the energy use of each device separately in an L-DED system [22]. They found that the power rates of the control cabinet, powder feed, and kinetic system were stable and significantly less than and cooling system and laser system. The cooling system,

however, runs stochastically and infrequently during the whole manufacturing process. It is noteworthy that the energy consumption on the process level primarily focuses on the laser system [23]. On one hand, the laser system is the most dominant contributor to the energy consumption of L-DED system. On the other hand, the energy distribution of laser energy exerted on the powder, substrate, and molten pool reflects the dynamic thermal history and quality of deposited layers.

The metallic material utilized in this study is Ti–10Mo powders with diameters in the range of 66.3–254 µm. Table 2 illustrated the chemical composition of Ti–10Mo, determined by an inductively coupled plasma emission spectrometer (Agilent 720 ES). To enhance the flowability of

**Table 3**

Process parameters and experimental results.

No.	P(W)	Vs(mm/s)	F(g/min)	DR (%)	$\theta(^{\circ})$	AR	$S_d(mm^2)$	$S_{re}(mm^2)$
1	500	7	6	0.07	60.89	2.58	0.639	0.058
2	800	7	6	0.17	46.46	2.95	0.942	0.198
3	1100	7	6	0.29	35.24	4.06	1.163	0.449
4	1400	7	6	0.46	32.4	4.82	1.116	0.872
5	500	10	6	0.04	51.7	2.88	0.358	0.035
6	800	10	6	0.23	33.95	3.93	0.623	0.196
7	1100	10	6	0.36	26.7	4.65	0.628	0.339
9	1400	10	6	0.5	24.78	5.78	0.701	0.615
8	500	13	6	0.06	35.65	4.53	0.223	0.029
10	800	13	6	0.33	32.25	4.57	0.415	0.217
11	1100	13	6	0.41	26.28	5.26	0.561	0.471
12	1400	13	6	0.55	19.09	6.41	0.554	0.729
13	500	16	6	0.09	34.4	4.23	0.213	0.054
14	800	16	6	0.35	28.13	5.31	0.355	0.199
15	1100	16	6	0.43	23	5.73	0.42	0.376
16	1400	16	6	0.56	22.85	6.56	0.49	0.638
17	500	19	6	0.06	26.59	4.45	0.192	0.043
18	800	19	6	0.36	17	5.83	0.263	0.176
19	1100	19	6	0.46	16.03	5.92	0.358	0.351
20	1400	19	6	0.58	23.7	6.74	0.38	0.253
21	500	7	8	0.08	73.88	1.71	0.847	0.068
22	800	7	8	0.09	55.53	2.48	1.149	0.218
23	1100	7	8	0.23	52.83	2.82	1.504	0.469
24	1400	7	8	0.29	42.82	2.94	1.814	0.771
25	500	10	8	0.05	50.73	2.48	0.447	0.058
26	800	10	8	0.09	48.22	2.61	0.962	0.166
27	1100	10	8	0.26	39.28	3.18	1.121	0.412
28	1400	10	8	0.29	33.31	3.63	1.202	0.605
29	500	13	8	0.04	45.01	3.04	0.362	0.039
30	800	13	8	0.24	36.94	3.87	0.523	0.243
31	1100	13	8	0.36	27.94	4.78	0.715	0.387
32	1400	13	8	0.45	25.37	5.29	0.735	0.587
33	500	16	8	0.08	36.89	3.49	0.251	0.048
34	800	16	8	0.21	33.1	3.98	0.44	0.118
35	1100	16	8	0.34	24.39	4.54	0.594	0.35
36	1400	16	8	0.43	28.68	5.14	0.651	0.601
37	500	19	8	0.13	28.53	4.43	0.189	0.041
38	800	19	8	0.22	23.65	4.45	0.362	0.138
39	1100	19	8	0.42	21.55	5.46	0.448	0.362
40	1400	19	8	0.45	18.45	5.78	0.457	0.449
41	500	7	10	0.05	72.49	1.57	0.817	0.055
42	800	7	10	0.03	65.36	1.67	1.568	0.187
43	1100	7	10	0.09	58.08	2.25	1.872	0.382
44	1400	7	10	0.27	56.85	2.54	2.077	0.783
45	500	10	10	0.05	71.75	2.06	0.61	0.086
46	800	10	10	0.09	54.05	2.44	0.993	0.226
47	1100	10	10	0.2	45.85	2.94	1.294	0.352
48	1400	10	10	0.37	36.51	3.53	1.217	0.717
49	500	13	10	0.08	56.33	2.94	0.348	0.086
50	800	13	10	0.21	51.85	3.52	0.608	0.166
51	1100	13	10	0.26	41.64	3.7	0.866	0.296
52	1400	13	10	0.48	34.33	4.84	0.77	0.708
53	500	16	10	0.04	55.87	2.69	0.392	0.033
54	800	16	10	0.19	47.89	3.47	0.616	0.168
55	1100	16	10	0.25	39.36	3.42	0.77	0.233
56	1400	16	10	0.42	32.39	4.68	0.847	0.496
57	500	19	10	0.08	39.58	3.54	0.262	0.054
58	800	19	10	0.26	29.03	4.3	0.4	0.15
59	1100	19	10	0.3	33.39	4.41	0.499	0.205
60	1400	19	10	0.45	26.67	5.13	0.495	0.293

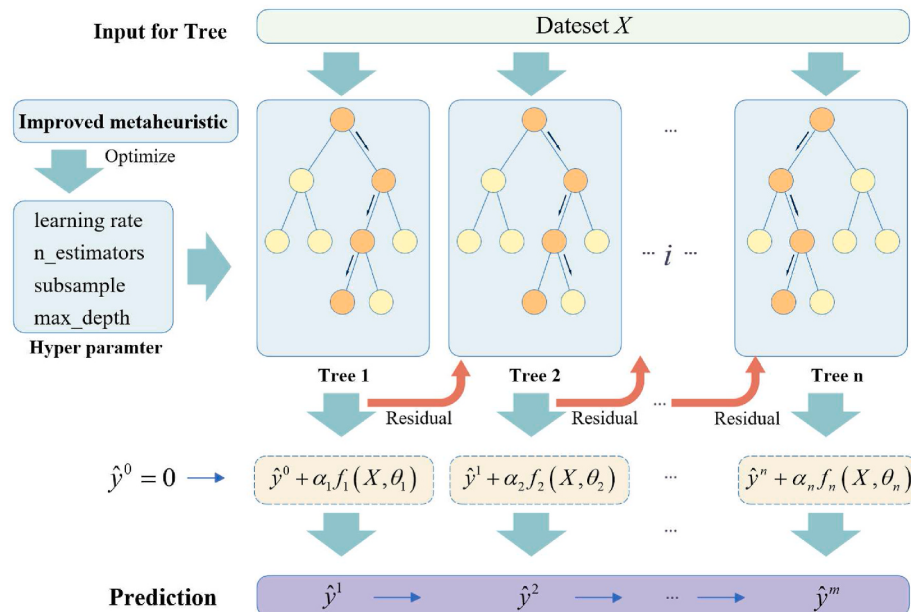


**Fig. 5.** Schematic diagram of original XGBoost.

the powder, the powder was dried at 105 °C for 2 h. Additionally, the TC4 titanium substrate (100 × 100 × 3 mm) was polished using sandpaper to eliminate surface impurities and oxide films. The laser beam spot size used in the experiment was 2 mm, and the printing length was 40 mm. The deposition laser head was positioned 13 mm above the substrate. To ensure a good metallurgical effect between the clad track and the substrate, preheating of the substrate was conducted with a laser power of 600W before each experimental group. The samples of deposited layers all belong to single-layer and single-track formations.

### 3.2. Geometrical performance metrics

This study selected three quality performance metrics for the deposited layers: wetting angle ( $\theta$ ), dilution rate (DR), and aspect ratio (AR). The last two can be calculated using the following equation:

$$DR = \frac{d}{d+h} \quad (9)$$

$$AR = \frac{w}{h} \quad (10)$$

where  $w$  is the width of deposited layer in mm,  $h$  is the height of deposited layer in mm, and  $d$  is the depth of molten area in mm, as shown in Fig. 3. Wetting typically refers to the behavior of a liquid infiltrating the interior of a solid or adhering to the surface of a solid. When the contact angles are large, this would result in a non-wetting circumstance and a tendency to adopt a circular shape to lower the surface area [24]. Thus, lower contact angles usually indicate better wetting. To provide outstanding wear resistance and corrosion resistance of the cladding layer, a reasonable minimum dilution rate is needed in practical applications. The ideal dilution rate differs for various materials. An extremely high dilution rate might reduce the cladding layer's quality and raise the risk of deformation and cracking [25]. On the other side, an over-low dilution rate might cause the cladding layer to delaminate [26]. AR of the deposited layer refers to the ratio between the width and height of its cross-section. An excessively high AR tends to cause porosity during the deposition process, lowering the effectiveness of overlaying. Conversely, an over-lower AR might induce inadequate wetting and a higher chance of flaws during the fabrication process, as well as poor metallurgical bonding between the deposition zone and the substrate [27].

Three processing parameters, i.e., the powder feed rate (F), scanning speed (Vs), and laser power (P) were varied at different levels. These three parameters have been proven to be significantly influential parameters to energy consumption [28,29]. We conducted a full factorial experiment with 60 sets of parameter combinations. The fabricated deposition layers were sliced by wire electrical discharge machining to obtain the corresponding 60 samples. Subsequently, we employed the metallographic mosaic method to further prepare the samples. Molybdenum sandpapers and diamond paste were utilized for the sanding and polishing processes. Additionally, an etchant was applied to reveal the fusion zones of the samples. With the geometry profile of cross sections observed by microscope (ICX41 M), we measured the deposited areas and remelted areas via manually drawn closed curves in the imageview software. The system inputs (processing parameters) and outputs data (geometrical performance metrics) for later performance prediction and optimization as shown in Table 3.

### 4. Algorithm description

#### 4.1. Framework of prediction using XGBoost with improved metaheuristics

The prediction objective of this study was based on the XGBoost. The XGBoost approach benefits from automatic parallel processing and adaptive tree topologies, which make it possible for it to efficiently handle large datasets in real-time [30]. The schematic diagram of XGBoost's decision tree construction process was presented in Fig. 5.

The construction of each decision tree aims to address the challenging samples that were predicted with relatively lower accuracy by the previous trees. As a result, every tree in XGBoost is thought of as a weak base learner. The ultimate prediction of the model can be explained by:

$$\hat{y}^m = \hat{y}^{m-1} + \alpha f_m(X, \theta_m) = \alpha \sum_{j=1}^m f_j(X, \theta_j) \quad (11)$$

where  $\alpha$  is the shrinkage factor in decision trees, which is used to control the learning rate of the fitting process;  $m$  is the number of decision trees;  $X$  is the predictor;  $\theta_j$  is a parameter that controls the structure of the  $j$ -th tree;  $f_j(X, \theta_j)$  is the output of the  $j$ -th decision tree based on the  $\theta_j$ .

structure without shrinkage and  $\hat{y}^j$  represents the prediction of the j-th decision trees. The predictor variables X and the residuals  $y - \hat{y}^{j-1}$  from the previous trees are used as inputs for constructing a new decision tree. As a result, as the quantity of decision trees increases, the residuals usually decrease. In the forward phase of the process, the objective function that needs to be optimized is:

$$\sum_i L(\hat{y}_i, y_i) + \sum_j \Omega(\theta_j) = \sum_i L\left[y_i, \hat{y}_i^{j-1} + af_j(X_i, \theta_j)\right] + \sum_j \Omega(\theta_j) \quad (12)$$

where L is the loss function, which is calculated as the squared error between the predicted value  $\hat{y}$  and the true value y. A greater number of leaves in a model typically reduces the error, but it can also lead to overfitting issues. To penalize the complexity of the model and prevent overfitting, a regularization term is introduced with:

$$\sum_j \Omega(\theta_j) = \varepsilon \cdot J_j + \frac{1}{2} \lambda \cdot \sum_{j=1}^J \omega_{jk}^2 \quad (13)$$

where  $J_j$  is the total number of leaf nodes in the j-th tree while  $\varepsilon$  and  $\lambda$  are regularization parameters;  $\omega_{jk}$  is the weight of the k-th leaf within the j-th tree. To facilitate the utilization of custom loss functions, XGBoost adopts a substitution of the loss function with a second-order Taylor expansion.

For optimal splitting at each node, the branch with the largest gain is chosen. During the process of tree pruning, a gain function is computed with:

$$\text{Gain} = \frac{1}{2} \left[ \frac{G_L^2}{H_L + \lambda} + \frac{G_R^2}{H_R + \lambda} - \frac{(G_L + G_R)^2}{H_L + H_R + \lambda} \right] - \gamma \quad (14)$$

where  $\gamma$  represents the structural complexity introduced by the splits;  $G_L$ ,  $G_R$ ,  $H_L$  and  $H_R$  represent the combined sum of  $g_i$  and  $h_i$  for the left and right branches following the split.

Extensive research has shown that hyperparameters play a crucial role in determining the final performance of XGBoost models [31]. Heuristic algorithms are typically problem-specific and rely on domain

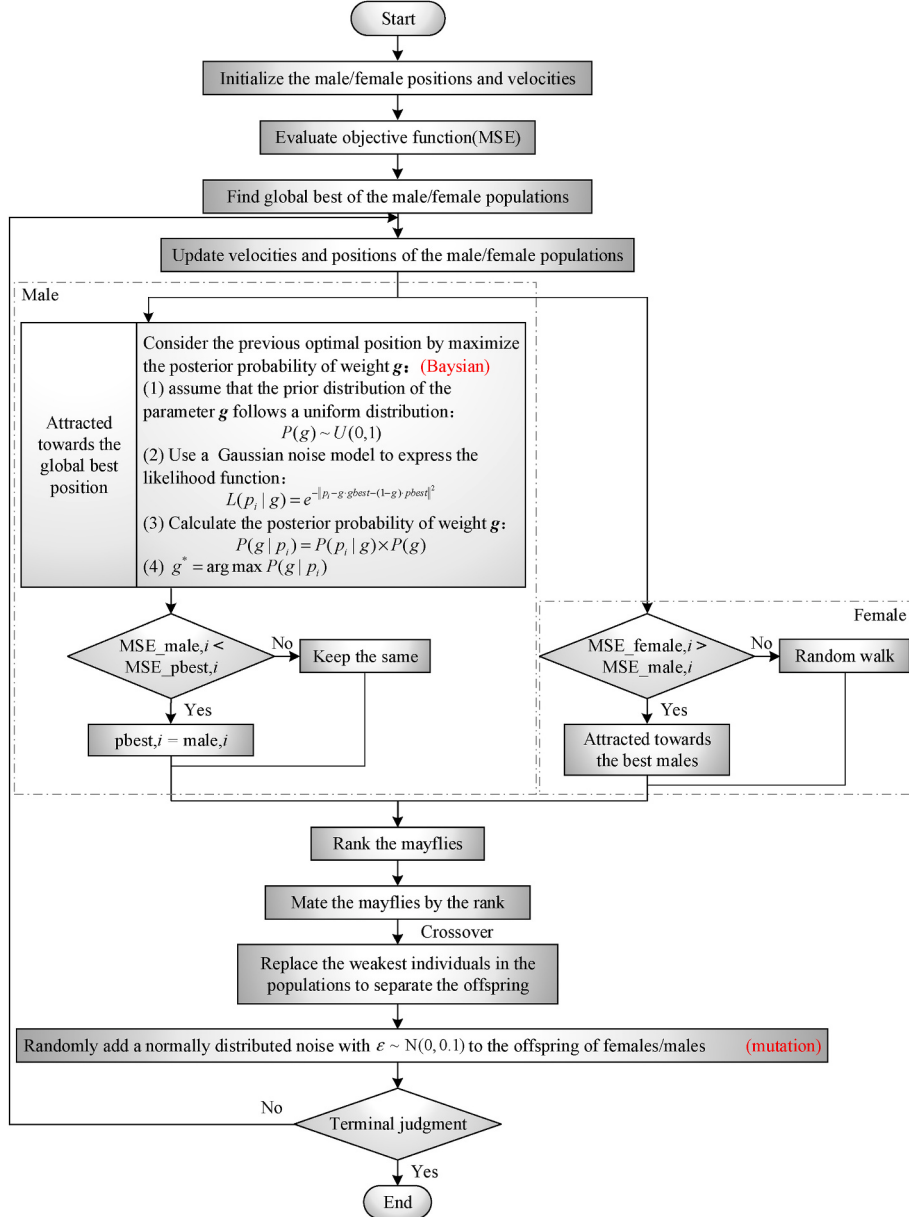


**Fig. 6.** Flow chart of improved MA with Bayesian technique and mutation strategy.

knowledge to guide the search process, whereas metaheuristics are higher-level frameworks that can be adapted to various optimization problems [32]. Therefore, we incorporated the Bayesian theory and mutation strategy into the meta-heuristic inspired by Mayfly. Such techniques enabled the identification of better hyperparameters in the original XGBoost, e.g., the learning rate, subsample, maximum depth (max\_depth), and number of decision trees (n\_estimators). Then its predictive accuracy was expected to be enhanced to some extent.

#### 4.2. Mayfly algorithm revisit

The Mayfly algorithm (MA) draws inspiration from the flight behavior and mating process observed in mayflies and is originally proposed by Ref. [33]. It can be regarded as a derivative of the particle swarm optimization (PSO) algorithm [34], firefly algorithm [35], invasive weed optimization [36], etc. The algorithm initializes two populations of mayflies, namely the male population and the female population, through a random generation process. Each mayfly's position within the search space represents a potential solution to the problem. The male and female populations of mayflies exhibit distinct movement strategies. Males' movement can be formulated as below:

$$x_i^{t+1} = x_i^t + v_i^{t+1} \quad (15)$$

$$v_{i,d}^{t+1} = v_{i,d}^t + c_1 e^{-\beta r_p^2} (pbest_{i,d} - x_{i,d}^t) + c_2 e^{-\beta r_g^2} (gbest_d - x_{i,d}^t) \quad (16)$$

where  $x_{i,d}^t$  is position of individual  $i$  on dimension  $d$  at step  $t$ ,  $v_{i,d}^t$  is velocity of individual  $i$  on dimension  $d$  at step  $t$ , and the flying direction of each mayfly is determined by a dynamic interplay of its individual flying experiences and the social interactions within the group.  $c_1$  and  $c_2$  are two constants associated respectively with the social and cognitive components,  $\beta$  is a fixed factor to limit the connectivity among individuals within the swarm.  $pbest_{i,d}$  is the personal best position achieved so far,  $gbest_d$  is the best position obtained by any mayfly in the  $N$  swarm. Furthermore,  $r_p$  and  $r_g$  is the Cartesian distance between  $x_i$  and its  $pbest$  and  $gbest$  respectively. The two factors are formulated as:

$$\|x_i - X_i\| = \sqrt{\sum_{j=1}^n (x_{ij} - X_{ij})^2} \quad (17)$$

where  $X_i$  is associated with  $pbest$  or  $gbest$ .

Females are attracted by superior males. Females' movement strategies can be formulated as:

$$y_i^{t+1} = y_i^t + v_i^{t+1} \quad (18)$$

$$v_{i,d}^{t+1} = \begin{cases} v_{i,d}^t + c_2 e^{-\beta r_{mf}^2} (x_{i,d}^t - y_{i,d}^t), & \text{if } f(y_i) > f(x_i) \\ v_{i,d}^t + fl * r, & \text{if } f(y_i) \leq f(x_i) \end{cases} \quad (19)$$

where  $y_{i,d}^t$  is the position of female individual  $i$  on dimension  $d$  at step  $t$ ,  $r_{mf}$  is the Cartesian distance between male and female individuals,  $fl$  is a random movement factor used when a female is not attracted by a male, and  $r$  is a random number with a range of [-1, 1].

The crossover operator models the mating process between two mayflies in the following manner: A single parent is chosen from the male population and another from the female population. The selection of parents mirrors the process in which females are attracted to males. Specifically, the selection can be either random or based on their fitness function. In the latter case, the highest-performing female mates with the highest-performing male, the second highest-performing female with the second highest-performing male, and so forth. The crossover operation produces two offspring, which are generated according to the followings:

$$\begin{cases} \text{offspring1} = L * \text{male} + (1 - L) * \text{female} \\ \text{offspring2} = L * \text{female} + (1 - L) * \text{male} \end{cases} \quad (20)$$

Where  $L$  is a random value within a specific range. The initial velocities of the offspring are initialized to zero.

In each iteration, a total of  $2N$  offspring are generated through the crossover operation. From this pool of offspring, the top  $N$  individuals with the highest fitness are selected to replace the current population. These selected individuals are then randomly divided into male and female groups, forming the new population for the next iteration. This strategy ensures that the population is continually refreshed with the most promising offspring, promoting the exploration and exploitation of the search space in subsequent iterations.

#### 4.3. MA with Bayesian techniques

While the velocity limit can restrict the mayflies from attaining excessive speeds, there are instances where it becomes necessary to decrease the velocities. This adjustment was made to effectively manage the trade-off between exploration and exploitation capabilities of the mayflies. To ensure that the MA algorithm possesses a convergence like PSO, we introduced a new inertia weight denoted as  $g_i^t$  to precede  $v_{i,d}^t$  in Eq. (16). This paper proposed a Bayesian MA method that incorporates a probability density function, and the procedure of algorithm was presented in Fig. 6.

The optimal inertia weight was determined by maximizing the posterior probability density function associated with the weight. Furthermore, considering the independence of data in each dimension of MA, the analysis in the subsequent discussion was focused on a single dimension. In summary, we simplified Eqs. (16) and (19), and made the following modifications:

$$V_i^{t+1} = g_i^t V_i^t + c_1 R_p (pbest_i - X_i^t) + c_2 R_g (gbest_i - X_i^t) \quad (21)$$

We also incorporated a constant denoted as  $g_c$  into Eq. (19), drawing inspiration from Eq. (16):

$$g_i^{t+1} = \begin{cases} g_c V_i^t + c_2 R_{mf} (X_i^t - Y_i^t), & \text{if } f(Y_i) > f(X_i) \\ g_c V_i^t + fl * r, & \text{if } f(Y_i) \leq f(X_i) \end{cases} \quad (22)$$

Bayesian was introduced to estimate the inertia weight  $g_i^t$ . Generally, it is challenging to obtain prior information about  $g_i^t$ , so we adopted a Uniform distribution to represent this prior. Gaussian noise model was introduced to express the likelihood function:

$$L(p_i | g_i^t) = e^{-\|p_i - g_i^t \cdot g_i^t \cdot pbest_i - (1 - g_i^t) \cdot pbest_i\|^2} \quad (23)$$

Then we calculated the posterior probability of weight  $P(g_i^t | p_i)$  and updated the individual weight  $g_i^{t+1}$ :

$$P(g_i^t | p_i) = P(p_i | g_i^t) \times P(g_i^t) \quad (24)$$

$$g_i^{t+1} = \text{argmax}_P(g_i^t | p_i) \quad (25)$$

#### 4.4. Mutation strategy

Premature convergence of MA can cause the algorithm to converge to a local minimum rather than a global minimum. To overcome this issue, we developed a modified version of the original algorithm incorporating a random mutation into a subset of the population. This mutation mechanism enables the algorithm to explore unexplored regions of the search space. Specifically, a normally distributed random number is added to the variable of the selected offspring for mutation. This random perturbation introduces variability and promotes exploration beyond the local optima. Consequently, the offspring underwent modifications as follows:

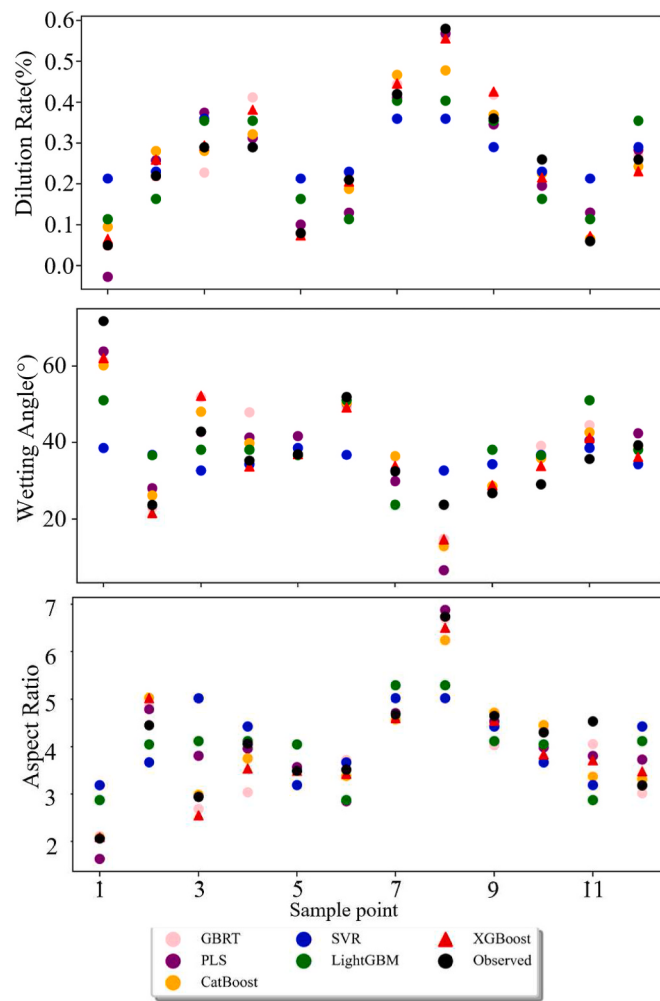


**Fig. 7.** Prediction comparison of popular machine learning algorithms.

**Table 4**

The cumulative sum of the absolute differences between predicted values and observed values across 12 groups for all features.

	GBRT	PLS	CatBoost	SVR	LightGBM	XGBoost
Dilution Rate (%)	0.39	0.52	0.38	0.96	0.87	0.36
Wetting Angle (°)	69.35	67.15	56.17	106.56	86.62	51.44
Aspect Ratio	3.30	4.36	3.21	10.30	9.09	3.61

$$\begin{cases} \text{offspring1} = L * \text{male} + (1 - L) * \text{female} + \varepsilon_1 \\ \text{offspring2} = L * \text{female} + (1 - L) * \text{male} + \varepsilon_2 \end{cases} \quad (26)$$

where  $\varepsilon$  follows a normal distribution with mean = 0 and variance = 1.

#### 4.5. Algorithms comparison and evaluation metrics

Among the various machine learning techniques, one needs to choose an appropriate algorithm to serve as the basic model. Popular machine learning models and statistical learning such as Support Vector Regression (SVR), Light Gradient Boosting Machine (LightGBM), Categorical Boosting (CatBoost), Partial Least Squares (PLS), Gradient Boosting Regression Tree (GBRT), and original XGBoost were trained and tested by the established dataset. The prediction performance of 12 testing samples was shown in Fig. 7. As shown in Table 4, in summarizing the cumulative sum of the absolute differences between predicted

values and observed values across 12 groups for all features, XGBoost mostly excelled, with only a minor shortfall to CatBoost in aspect ratio predictions, yet this gap was slight. We selected the XGBoost as the model basis, considering its prediction values (red triangle) were close to the observed values (black circle) in most cases.

To further validate the prediction performance of the proposed approach, we integrated PSO, MA, Bayesian technique, or Bayesian-MA into the XGBoost separately, also called N-XGBoost in this study, as a comparative basis. Hereby, the 'N' in 'N-XGBoost' refers to PSO, MA, Bayesian, Bayesian-MA, and improved MA (the MA with Bayesian and mutation strategy). Data in Table 3 were randomly divided into two sections for training and testing purposes. 80 % of the total samples were used to train the N-XGBoost model using a ten-fold cross-validation approach, and the remaining 20 % were used to verify the accuracy of models.

All these algorithms were evaluated based on statistical criteria including R-squared ( $R^2$ ), Mean Absolute Error (MAE), Mean Square Error (MSE), and Mean Absolute Percentage Error (MAPE).  $R^2$  measures the proportion of the variance in the dependent variable that can be explained by the independent variables in a regression model. It indicates how well the regression model fits the observed data. MAE measures the average absolute difference between the predicted and actual values. MSE is the average squared difference between the predicted and actual values. MAPE measures the average percentage difference between the predicted and actual values and provides a relative measure of the model's accuracy. Higher  $R^2$  implies better-explained variance of the model. Whereas lower MAE, MSE, and MAPE mean better predictive accuracy. MAE is usually less sensitive to outliers compared to other metrics like MSE. These criteria can be calculated by:

$$R^2 = 1 - \frac{\sum (y_{i,obs} - y_{i,pred})^2}{\sum (y_{i,obs} - \hat{y})^2} \quad (27)$$

$$MAE = \frac{1}{n} \sum_{i=1}^n |y_{i,obs} - y_{i,pred}| \quad (28)$$

$$MSE = \frac{1}{n} \sum_{i=1}^n (y_{i,obs} - y_{i,pred})^2 \quad (29)$$

$$MAPE = \frac{100\%}{n} \sum_{i=1}^n \left| \frac{y_{i,obs} - y_{i,pred}}{y_{i,obs}} \right| \quad (30)$$

where  $n$  is the number of observations,  $\hat{y}$  is the mean observed value,  $y_{i,obs}$  and  $y_{i,pred}$  are the  $i$ -th observed and predicted values, respectively.

#### 4.6. Multi-objective optimization construction

Both the relationship between SEC and EUR as well as the connection between energy efficiency and the geometry of deposited layers are intricate. Although in "black box" form, the above-mentioned meta-heuristics method in combination with machine learning could disclose the relationship between processing parameters, energy efficiency, and geometrical appearance. The optimization objectives in this study were to minimize the two energy efficiency indicators subject to the constraints of geometrical performances. Although both SEC and EUR represent the energy efficiency of AM, high EUR does not necessarily mean lower SEC under certain processing parameters, and vice versa. Over high or low wetting angle, dilution rate, and aspect ratio are not allowed because they would deteriorate the mechanical characteristics. Additionally, the processing parameters were also confined to certain ranges. Therefore, the multi-objective optimization problem can be expressed as below:

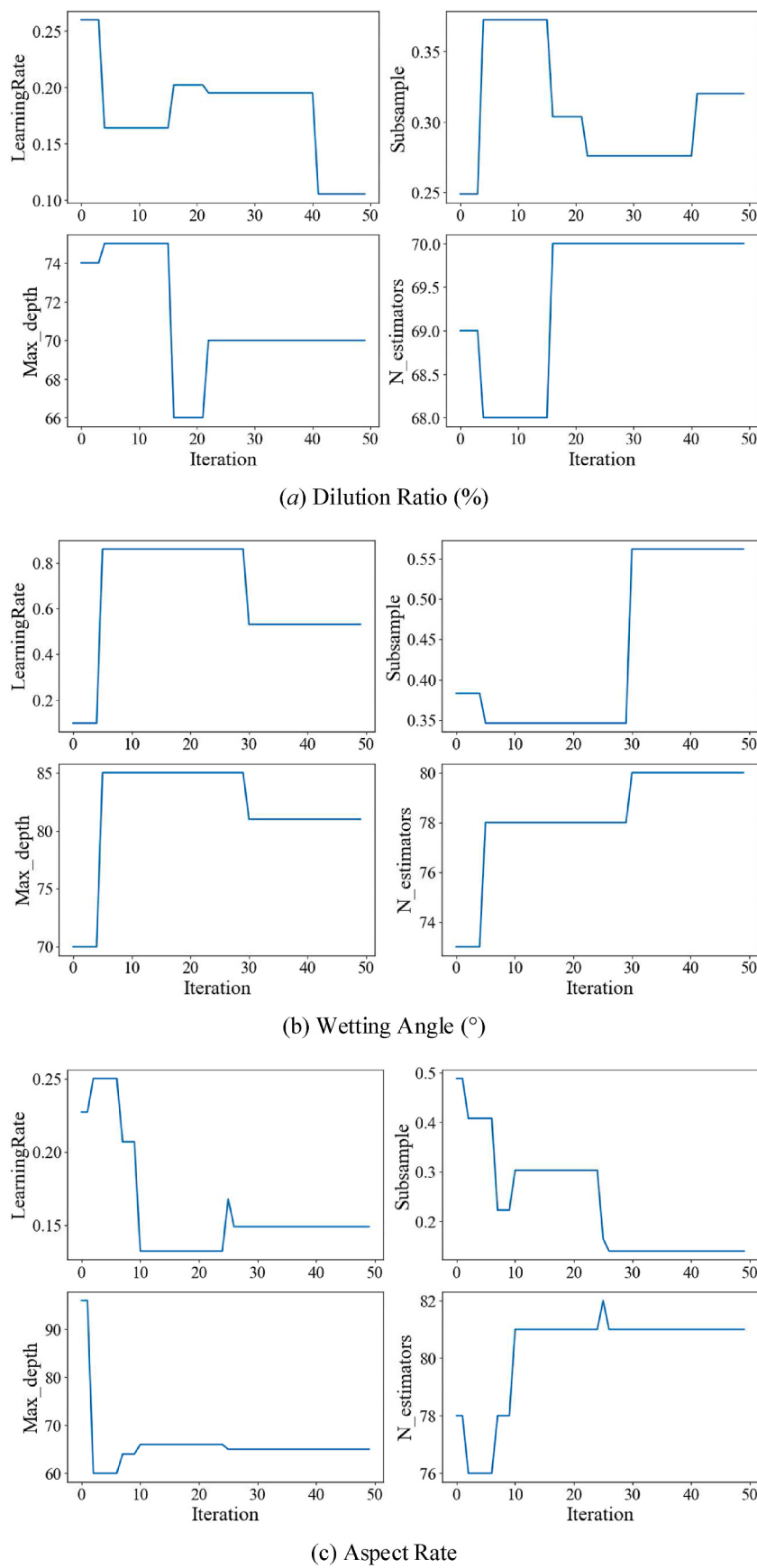
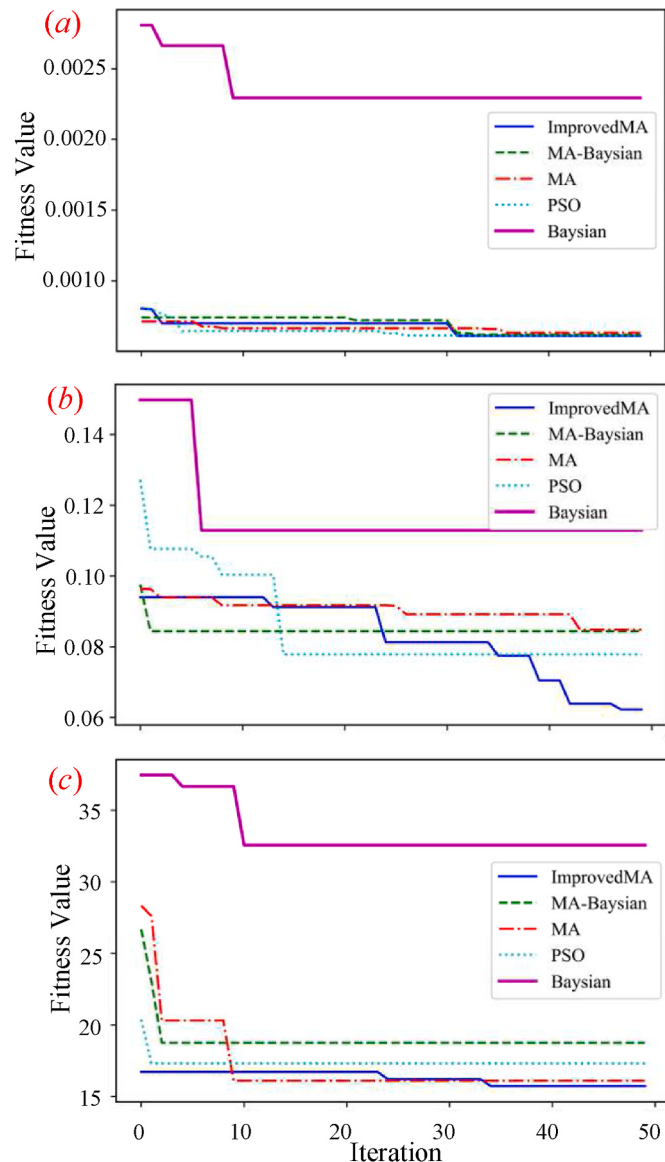


Fig. 8. Variation of hyperparameters during iterations.

**Table 5**

Final hyperparameters in the improved MA-XGBoost.

Geometry	Learning_rate	Subsample	Max_depth	N_estimators
Dilution Ratio(%)	0.1055	0.3201	70	70
Wetting Angle(°)	0.5319	0.5620	81	80
Aspect Rate	0.1489	0.1400	65	81

**Fig. 9.** Convergent curves of N-XGBoost for predicting: (a) DR, (b)  $\theta$ , and (c) AR.

$$\begin{aligned} \text{obj. } & \max \text{ ERU, } - \text{SEC} \\ \text{s.t. } & \left\{ \begin{array}{l} 30 \leq \theta \leq 90 \quad (\circ) \\ 10\% \leq DR \leq 30\% \\ 2 \leq AR \leq 4 \\ 500 \leq P \leq 1400 \quad (\text{W}) \\ 6 \leq Vs \leq 20 \quad (\text{mm/s}) \\ 6 \leq F \leq 10 \quad (\text{g/min}) \end{array} \right. \end{aligned}$$

We employed the NSGA-II to solve this optimization problem. NSGA-II was recognized as one of the most effective algorithms for multi-objective optimization, considering its efficient approximation of the Pareto border between various objectives [37]. The primary processes of this algorithm are fitness assessment, non-dominated sorting, crowding distance computation, selection, crossover, and mutation. Details on NSGA-II can be found in Ref. [38]. The  $\theta$ , DR, and AR predicted from the improved MA with the Bayesian technique and mutation strategy were used to determine the fitness values for each generation of NSGA-II.

## 5. Computational results

### 5.1. Geometrical performance prediction with N-XGBoost

To validate the superiority of improved MA-XGBoost, we attempted to compare the performance of N-XGBoost in the prediction of DR,  $\theta$ , and AR. Due to space limitations, we would only focus on geometrical metrics in this section, excluding energy efficiency metrics hereby. All these algorithms run on an identical computational platform. The 'N' part in N-XGBoost aims at finding the optimal hyperparameters to improve the prediction accuracy of the original XGBoost. In the example of improved MA-XGBoost, Fig. 8 showed intermittent variations of four hyperparameters across 50 training iterations. The final hyperparameters tend to converge and can be regarded as optimal ones. After the training process, the final hyperparameters shown in Table 5 were adopted for the prediction of geometrical indicators.

The convergent curves of N-XGBoost were presented in Fig. 9. It was evident that the proposed improved MA-XGBoost outperformed others in terms of convergence rate and fitness value. The fitness value is a measurement derived from the fitness function in meta-heuristic algorithms, which is comparable to the loss function in machine learning methods. This demonstrated the superiority of MA-XGBoost in fitting accuracy and efficiency. The MA-Bayesian XGBoost showed competitive performance, as the Bayesian technique constantly updated the prior information, and a limited number of iterations for parameter tuning facilitated the search speed. Compared with improved MA-XGBoost, the absence of mutation strategy in MA-Bayesian XGBoost limited its exploration capability in feasible space. Exclusively incorporating the PSO into XGBoost also presented good fitting accuracy and convergence rate. Comparison with Bayesian-XGBoost indicated that the meta-heuristic algorithm was an ideal option to modify the hyperparameters in the machine learning model.

We adopted 12 samples of processing parameters and corresponding geometrical indicators to test the prediction accuracy of N-XGBoost. As clear from Figs. 10–12, improved MA-XGBoost has the largest  $R^2$  and least MSE, indicating the proposed model demonstrated a strong ability to explain the variation in the dependent variable and achieves accurate predictions with minimal errors. In the case of  $\theta$  prediction (Fig. 12), the MAE and MAPE of improved MA-XGBoost were slightly greater than that of MA-Bayesian XGBoost. This implied that improved MA-XGBoost has a stronger ability to capture overall trends but may have a slightly less accurate predicting capability in specific cases. Whereas the proposed model still possessed the best performance in terms of MAE and MAPE for predicting AR (Fig. 10) and DR (Fig. 11).

In XGBoost, feature importance quantifies the relative importance of each feature in predicting the target variable. It is based on their

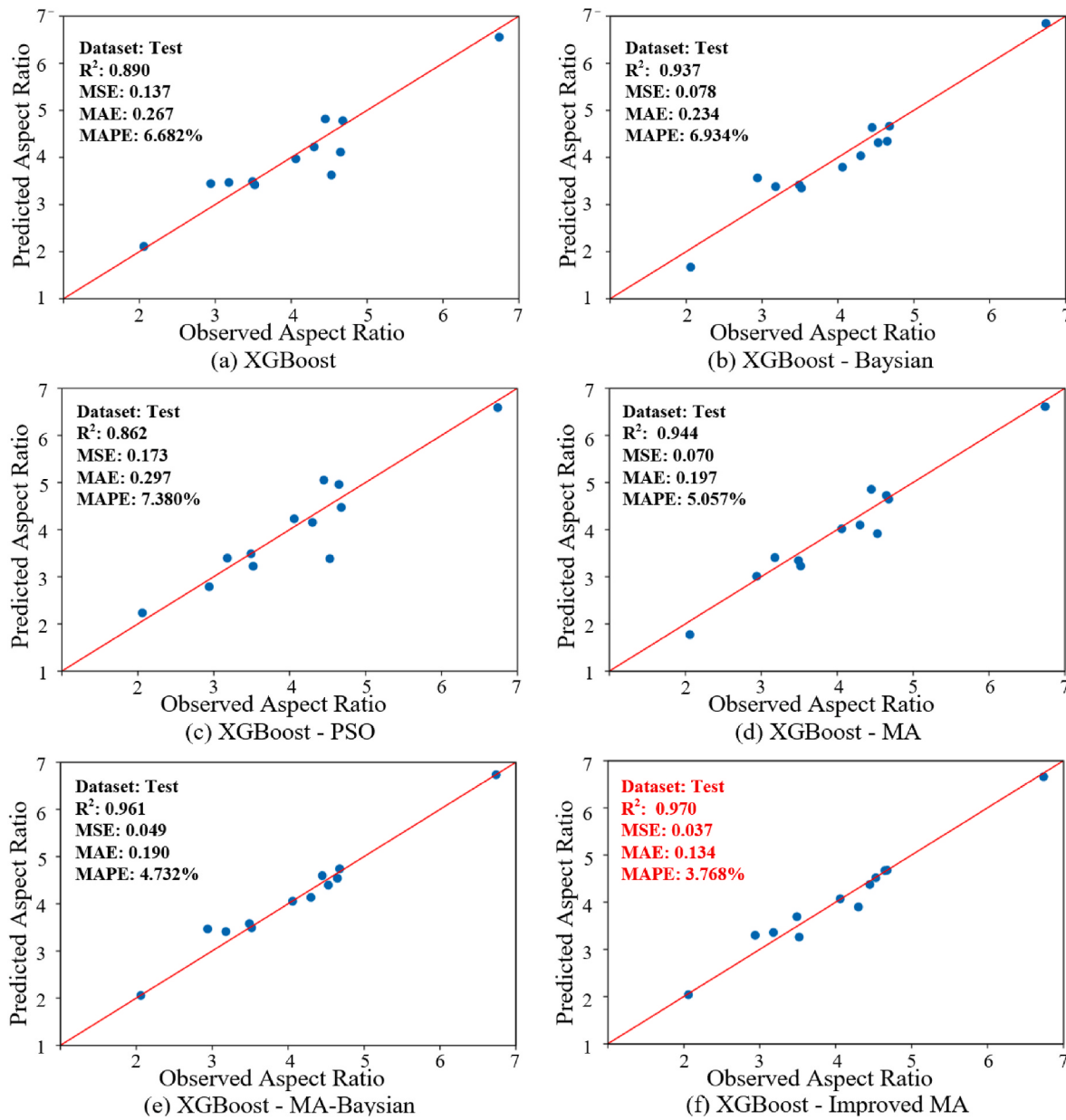


Fig. 10. Comparison of N-XGBoost for predicting AR (training phase).

frequency and importance in decision trees during boosting. Higher values indicate greater importance, with scores normalized, to sum up to 1. The relevance of a feature is expressed by its weight, which measures how frequently it is used across all trees. A larger weight indicates that the feature is utilized in more trees and contributes more significantly to the outcome of the prediction, reflecting the importance of the feature. It helps rank and identify influential features for predictions.

Shapley Additive exPlanations (SHAP) method, a technique used to explain the output of ML models, was utilized in this study [39]. Fig. 13 showed the relevant importance of the processing parameters on the geometric appearance and energy efficiency determined by the prediction model in this study. It indicated that the laser power had the greatest impact on the dilution rate, with the effects of powder feed rate and scanning speed having relatively lesser but comparable effects. Similar reactions to the processing parameters may be observed for the wetting angle and aspect ratio, with scanning speed having the biggest influence, followed by powder feed rate, and laser power having the smallest influence, which was consistent with the actual situation. Higher laser power directly influences the melting and solidification of

the deposition track, affecting both its size and exerting an influence on the dilution rate observed in the track. Lower scanning rates result in longer molten pool dwell durations, whilst higher speeds result in shorter stay times. This difference in scanning speed reflected the length of the molten pool. This affects the accumulation of metal powder during the deposition process, which in turn affects the wetting angle and aspect ratio. The process parameters produce different effects on EUR and SEC in terms of energy efficiency. The two factors that had the highest effects on EUR were the powder feed rate and scanning speed, whereas laser power had the least impact. The impact of the process parameters on SEC showed an opposite pattern on EUR.

## 5.2. Multi-objective optimization with NSGA-II

Table 6 listed the main parameters of NSGA-II. The EUR and SEC are not positively correlated, and a trade-off is required for energy conservation in L-DED process. To maximize both EUR and SEC, a bi-objective optimization using the NSGA-II algorithm was conducted. Instead of seeking a single optimal solution, the goal was to identify a set of

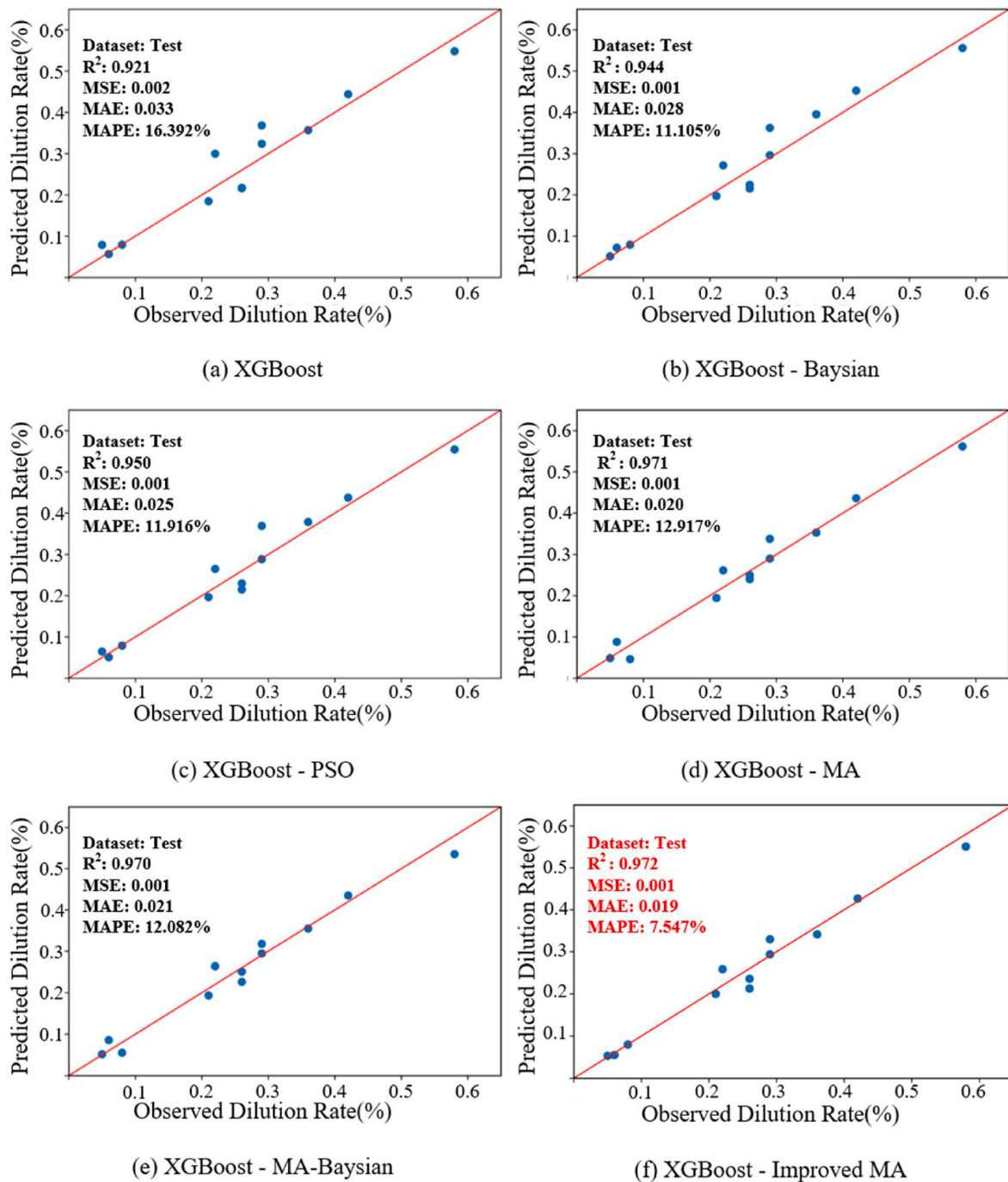


**Fig. 11.** Comparison of N-XGBoost for predicting DR (training phase).

optimal solutions known as the Pareto front. The Pareto front is referred to as the ideal situation where no objective can be further enhanced without unfavorable impact on other objectives. Each sample point at the Pareto front signifies a non-dominated solution [40]. The Pareto front for the processing parameters in the design space is shown in Fig. 14 by the blue sample points. For example, under the EUR of 18.43 %, the lowest SEC would be 3625.49 J/g. This nondominated solution implies that the laser power of 781 W, scanning speed of 12 mm/s, and powder feed rate of 10 g. In general, the Pareto front offers an ideal solution space for processing parameters, enabling flexible acquisition of parameters in actual AM practice with minimal energy consumption and good geometrical appearance.

In order to obtain deposited layer with rational geometrical

appearance, 15 satisfied layers were selected from a total of 60 sets of melted SEC and EUR values obtained under the constraints defined by Equation (27) and utilizing the process parameters provided in Table 3. The red dot in Fig. 14 represents the average energy efficiency values of these chosen layers, which were determined to be (16.88 %, 3713.50J/g), and correspondingly select the SEC solution corresponding to EUR of 16.88 % from the Pareto front (green dot in Fig. 14), and the EUR solution corresponding to SEC of 3717.50J/g (yellow dot in Fig. 14). The verification experiments were performed with these two sets of corresponding processing parameters. The cross-sectional results of the deposited layer for the verifying experiments are shown in Fig. 15. Table 7 displays the corresponding optimal values and experimental outcomes. The maximal relative error of EUR is –2.24 %, while that of

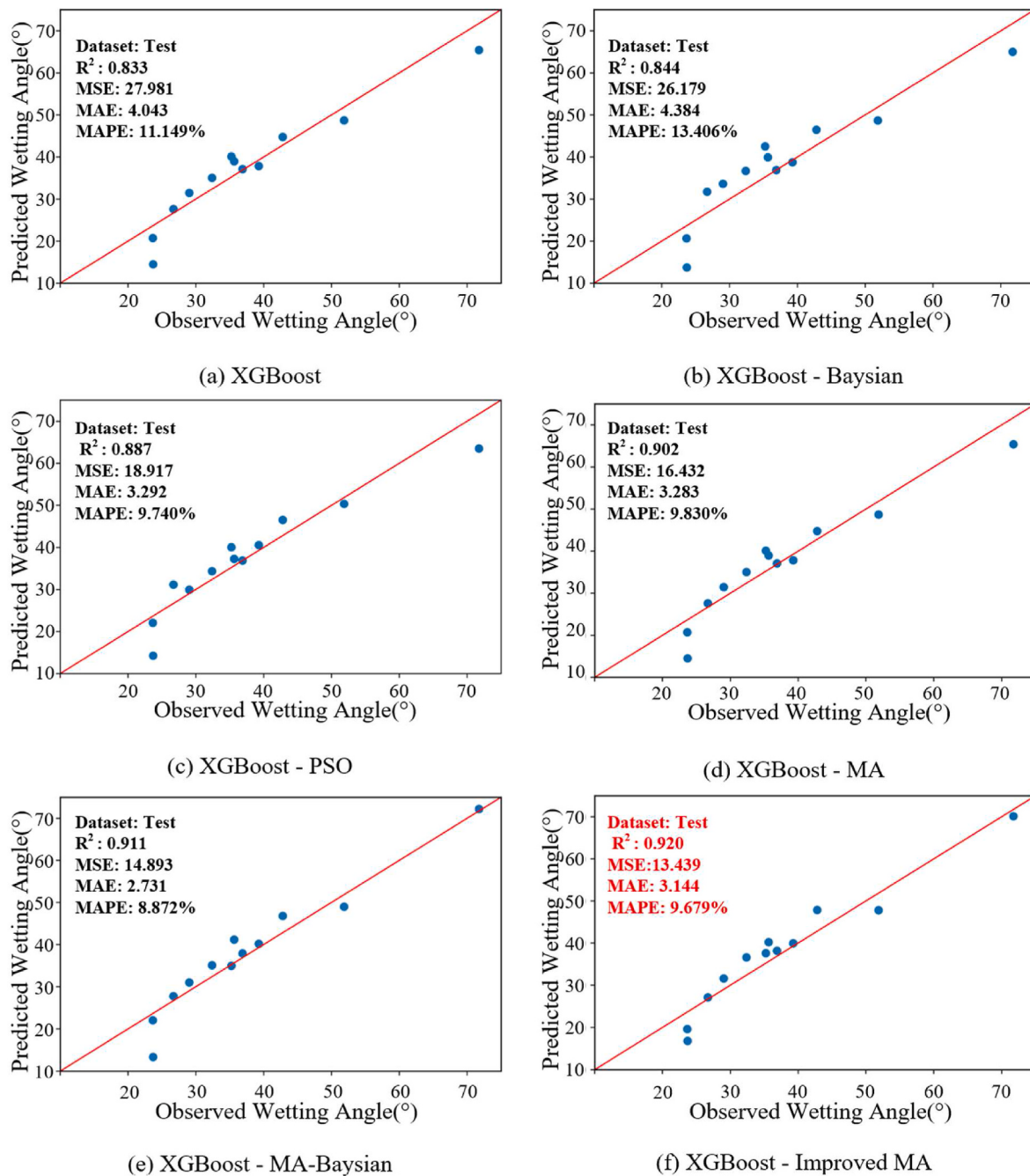


**Fig. 12.** Comparison of N-XGBoost for predicting  $\theta$  (training phase).

SEC is 2.06 %. These relative inaccuracies could be brought on by permissible factors like process variations and device accuracy restrictions. Compared with the average values of EUR and SEC of the satisfied deposited layer, the SEC experimental value of the optimal solution in Table 7 decreased by 2.1 % (from 3713.50J/g to 3637.15J/g) concerning that EUR was determined to be 16.54 %. While the experimental EUR value increased by 28.66 % (from 16.88 % to 23.66 %) concerning that SEC was determined to be 3791.56J/g, resulting in a greater improvement in energy efficiency. The selection of parameters from the Pareto front is a critical step that requires careful consideration of the relative importance of various indicators. For instance, if SEC is prioritized during the selection process, characteristics that result in lower SEC would be considered first. Additionally, a thorough analysis of trade-offs between various goals is feasible based on the Pareto front. One could assess the effects of parameter changes on energy usage,

geometrical appearance, and other pertinent factors. We chose optimal parameters from the Pareto front and ultimately achieve better results in terms of energy efficiency and geometrical appearance in AM practices while considering the preferential energy efficiency indicator in specific applications.

## 6. Implications and discussions

Increasing amounts of companies across almost every industry commit to carbon neutrality in decade(s) ahead. The current smart manufacturing can be no exception and still faces a rising need to reduce energy intensity and mitigate environmental impacts [41,42]. AM is a critical enabler for smart manufacturing from the perspective of manufacturing transformation (design freedom, decentralized and rapid-prototyping paradigm) [1] and intelligent sensor fabrication

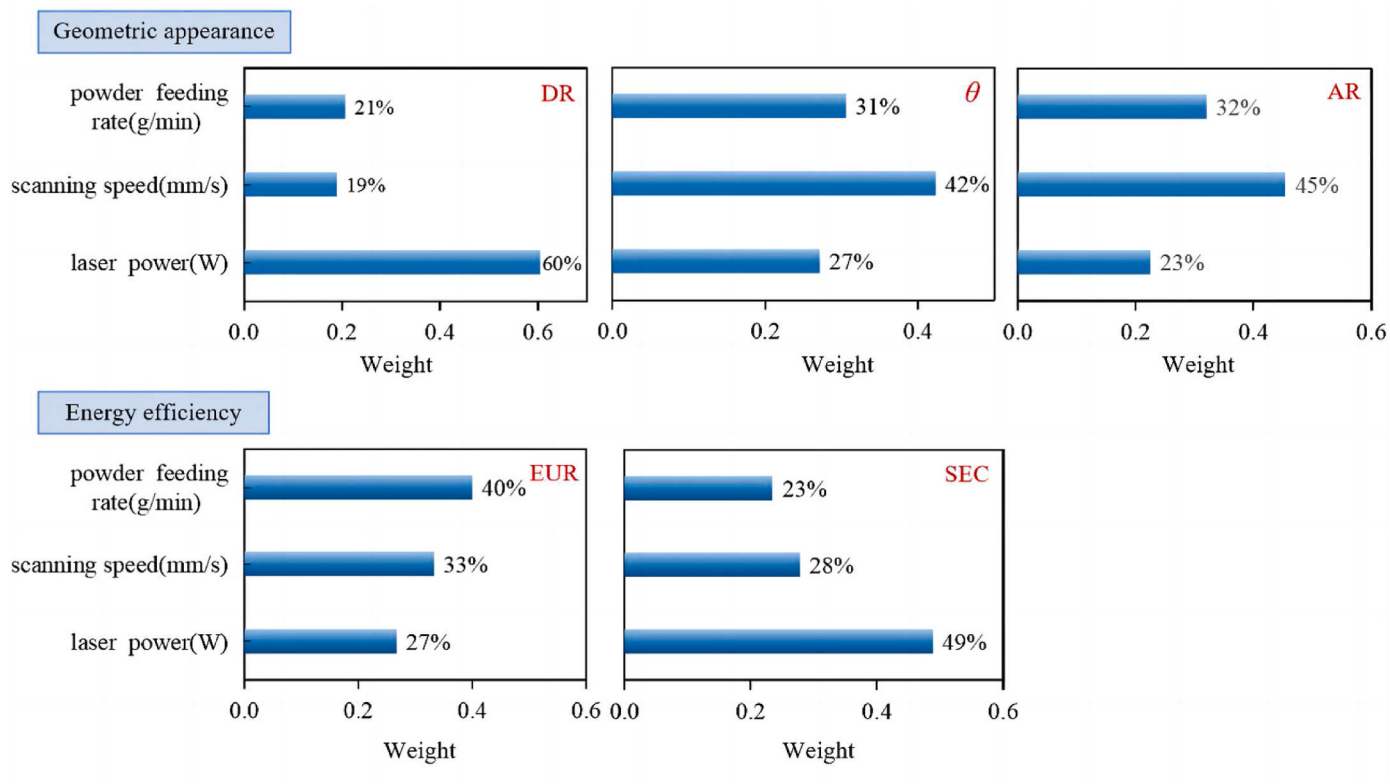


Fig. 13. Importance ranking of features.

**Table 6**  
Main parameters of NSGA-II.

Parameters	max_gen	pop_size	crossover_prob	mutation_prob	tournament_size
Values	2000	48	0.5	0.1	6

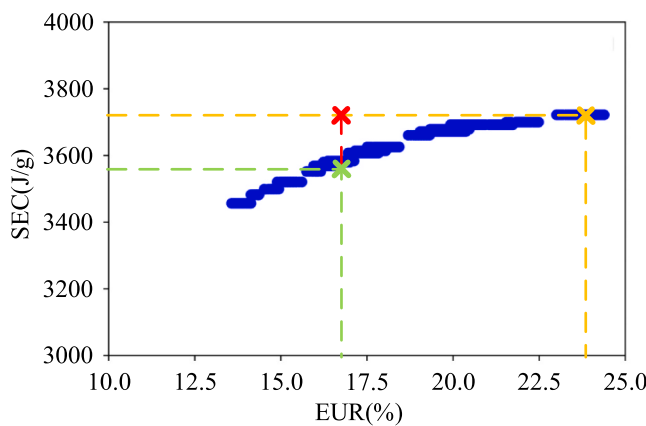


Fig. 14. Pareto front for energy efficiency in L-DED.

(flexible, low-cost, and reliable electronics) [43]. As the AM has gained the reputation of zero-waste in the manufacturing process, it seems environmentally friendly at first glance compared with traditional manufacturing techniques. This perception however probably misleading when the transparent lifecycle conditions, e.g., the geometry and materials of components are out of consideration. Compared with conventional subtractive manufacturing such as milling and turning, the estimated SEC values of AM process are approximately 1–2 orders of

magnitude higher [44]. The energy efficiency issue remains a barrier to the widespread and massive adoption of metal AM.

The manufacturing process is the dominant contributor to the life-cycle environmental burdens of AM. While the processing parameters remarkably affect the quality and energy consumption of metal AM given specific printing conditions like equipment, feedstock materials, and part orientation [45,46]. Additionally, the manufacturing process of typical AM itself is fairly slow, resulting in higher energy intensity. The processing parameters influence the production rate significantly and further determine the total energy consumption during the parts fabrication process. Energy consumption and mechanical properties of fabricated parts are closely related production criteria for AM. Although the effects of laser energy input exerted on microstructure formation and mechanical properties have been quantitatively analyzed in previous studies [3,47], the underlying mechanisms regarding energy density, heat flux, and crystal structure are complicated, prohibiting accurately prediction of energy use and mechanical properties solely from the mechanism perspective. However, machine learning techniques are promising alternatives to understanding and predicting the mechanical performance and energy consumption of AM without prior knowledge of interactive mechanisms between energy input and mechanical properties. These prediction and optimization approaches are feasible for energy conservation in AM practices.

The SEC of L-DED at the process level ranged from ~3400 to 4000 J/g, in line with the statistical analysis of SEC during AM processes by Ref. [5]. The range scope implied the potential for improvement via the optimization of processing parameters. It is worth noting that a considerably lower SEC does not necessarily suggest better performance.

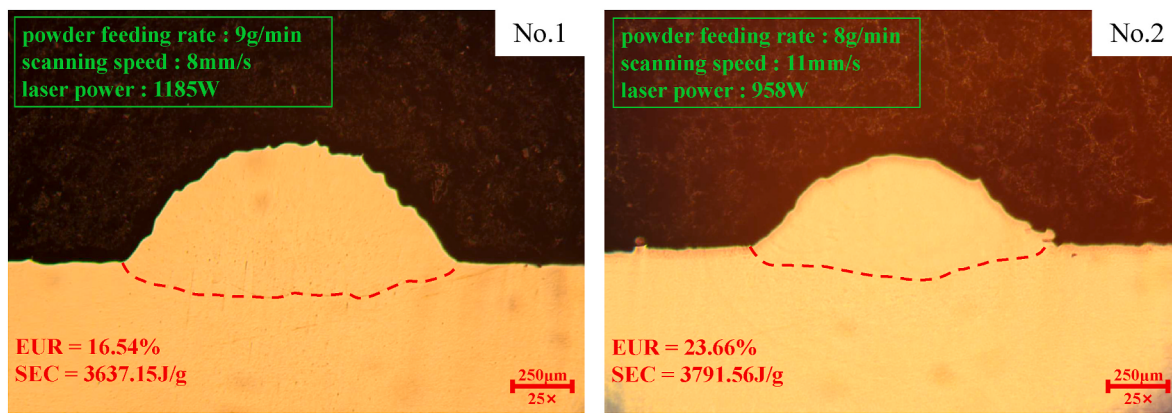


**Fig. 15.** The cross-sectional topography of two optimal solutions.

**Table 7**  
Processing parameters and results of verifying experiments.

No.	P (W)	Vs (mm/s)	F (g/min)	Value	EUR (%)	SEC (J/g)
1	1185	8	9	optimal	16.88	3583.35
				experiment	16.54	3637.15
				err.	-2.06 %	1.48 %
2	958	11	8	optimal	24.19	3713.50
				experiment	23.66	3791.56
				err.	-2.24 %	2.06 %

For example, high energy input in conjunction with higher scanning speed intuitively causes a greater mass of deposited layer and lower SEC but unqualified dilution rate. EUR was adopted in this study as a supplementary indicator of energy efficiency, characterizing the proportion of useful energy devoted to the metal deposition process. The combination of these two indicators can evaluate the energy efficiency of AM more comprehensively, preventing the excessive fusion bonding between two adjacent deposited layers [3].

The lifecycle energy footprint can be improved at multiple life cycle phases while optimizing the processing parameters at the manufacturing stage is a relevant and cost-effective method to enhance the environmental sustainability of AM. In the present study, the SEC and EUR were improved by 76.35 J/g and 6.78 %, respectively. This is essentially a significant improvement from merely an energy perspective. But the quality of AM parts should be considered with more priority. Notably, energy conservation of AM is performed with the prerequisite of quality assurance. From 2021 to 2028, a forecasted 21 % annual growth rate for the global AM market is expected [48]. The rising market indicated a substantial potential for energy saving through the optimization of AM process. Further, such prediction and optimization approaches can be easily extended to other AM forms such as selective laser sintering, electron beam melting, and fused deposition modeling.

## 7. Conclusions

The energy intensity of AM has been substantially greater than the traditional subtractive manufacturing, and the slow process rate of AM arguably further exacerbates this phenomenon. Fully exploiting the energy conservation potentials without compromising the quality performance has been greatly desired in AM practices. To collect the energy efficiency and geometrical appearance of deposited layers including wetting angle, dilution rate, and aspect ratio, the present study conducted a full factorial L-DED experiment under various combinations of processing parameters. We proposed an improved MA with Bayesian technique and mutation strategy and integrated it into XGBoost for determining better hyperparameters. NSGA-II was then applied to optimize the two energy efficiency indicators under the constraint of

feasible geometrical appearance.

The comparison amongst the prediction models indicated that improved MA-XGBoost overperformed others in terms of convergence rate and fitness values in the training process. Whereas in the prediction/testing process, improved MA-XGBoost had the largest  $R^2$  and least MSE, which proved its best accuracy compared with other N-XGBoost algorithms in predicting the geometrical appearance. According to a ranking of feature importance, the EUR was most affected by the powder feeding rate. The wetting angle and aspect ratio were mainly impacted by scanning speed. The dilution rate and SEC were primarily impacted by laser power. We also utilized the NSGA-II to trade off EUR and SEC indicators. The Pareto front of the L-DED process, a set of nondominated solutions, was found for ensuring the geometrical appearance of the deposited layers. The verifying experiments demonstrated that the error of Pareto curve was within 2.2 %.

This study could help provide optimal parametric combinations of L-DED from the perspective of energy consumption, supporting the selection of appropriate processing parameters without compromising the quality of parts. Additionally, as the present study primarily focused on the L-DED, the energy conservation strategy can be applied to other AM processes such as electron beam melting and selective laser melting. Wide application of energy-saving techniques in AM process also implies significant decreases in financial expenses and environmental impact.

As the prediction performance of machine learning algorithms is closely related to the size of the dataset, increasing the number of experiments is expected to level up the prediction accuracy. Considering that L-DED experiments are prohibitive for substantial amounts of trials, how to improve the performance of algorithms under a limited dataset should be explored in future work. Considering that this study is only limited to single-layer single-track experiments, follow-up studies can consider the multi-layer or multi-track situations as the thermal history, quality condition, and energy efficiency could be significantly complex in that cases. Since the AM processes are influenced by more than one hundred factors, additional features, e.g., the hatch spacing and laser spot size included in the training models would be desirable in the future studies.

## Data availability

Data will be made available on request.

## CRediT authorship contribution statement

**Baoyun Gao:** Conceptualization, Software, Writing – original draft. **Shitong Peng:** Funding acquisition, Supervision, Writing – review & editing. **Tao Li:** Methodology. **Fengtao Wang:** Data curation, Funding acquisition. **Jianan Guo:** Funding acquisition, Methodology. **Conghu Liu:** Validation. **Hongchao Zhang:** Formal analysis.

## Declaration of competing interest

The authors declare that they have no known competing financial interests or personal relationships that could have appeared to influence the work reported in this paper.

## Data availability

Data will be made available on request.

## Acknowledgement

We appreciate the financial support from the National Natural Science Foundation of China (Grant No. 52305544 and 52205110), Project of Guangdong Science and Technology Innovation Strategy (Grant No. STKJ202209065), Guangdong Provincial University Innovation Team Project (Grant No. 2020KCXTD012), and the 2020 Li Ka Shing Foundation Cross-Disciplinary Research (Grant No. 2020LKSFG01D).

## References

- [1] Mehrpouya M, Dehghanhadikolaei A, Fotovati B, Vosooghnia A, Emamian SS, Gisario A. The potential of additive manufacturing in the smart factory industrial 4.0: a review. *Appl Sci* 2019;9:3865. <https://doi.org/10.3390/app9183865>.
- [2] Seo G, Ahsan MdR, Lee Y, Shin J-H, Park H, Kim DB. A functional modeling approach for quality assurance in metal additive manufacturing. *Rapid Prototyp J* 2021;27:288–303. <https://doi.org/10.1108/RPJ-12-2018-0312>.
- [3] Liu W, Wei H, Liu A, Zhang Y. Multi-index co-evaluation of metal laser direct deposition: an investigation of energy input effect on energy efficiency and mechanical properties of 316l parts. *J Manuf Process* 2022;76:277–90. <https://doi.org/10.1016/j.jmapro.2022.02.016>.
- [4] Gutowski T, Jiang S, Cooper D, Cormier G, Hausmann M, Manson J-A, et al. Note on the rate and energy efficiency limits for additive manufacturing: rate and energy efficiency limits for AM. *J Ind Ecol* 2017;21:S69–79. <https://doi.org/10.1111/jiec.12664>.
- [5] Jackson MA, Van Asten A, Morrow JD, Min S, Pfefferkorn FE. Energy consumption model for additive-subtractive manufacturing processes with case study. *Int J Precis Eng Manuf-Green Technol* 2018;5:459–66. <https://doi.org/10.1007/s40684-018-0049-y>.
- [6] Peng S, Li T, Wang X, Dong M, Liu Z, Shi J, et al. Toward a sustainable Impeller production: environmental impact comparison of different Impeller manufacturing methods: environmental comparison of Impeller manufacturing. *J Ind Ecol* 2017;21:S216–29. <https://doi.org/10.1111/jiec.12628>.
- [7] Gedda H, Powell J, Wahlström G, Li W-B, Engström H, Magnusson C. Energy redistribution during CO2 laser cladding. *Int Congr Appl Lasers Electro-Opt 2001*.
- [8] Unocic RR, DuPont JN. Process efficiency measurements in the laser engineered net shaping process. *Metall Mater Trans B* 2004;35:143–52. <https://doi.org/10.1007/s11663-004-0104-7>.
- [9] Liu W, Wei H, Huang C, Yuan F, Zhang Y. Energy efficiency evaluation of metal laser direct deposition based on process characteristics and empirical modeling. *Int J Adv Manuf Technol* 2019;102:901–13. <https://doi.org/10.1007/s00170-018-03220-w>.
- [10] Oliveira JP, Santos TG, Miranda RM. Revisiting fundamental welding concepts to improve additive manufacturing: from theory to practice. *Prog Mater Sci* 2020;107:100590. <https://doi.org/10.1016/j.pmatsci.2019.100590>.
- [11] Kasperovich G, Haubrich J, Gussoni J, Requena G. Correlation between porosity and processing parameters in TiAl6V4 produced by selective laser melting. *Mater Des* 2016;105:160–70. <https://doi.org/10.1016/j.matdes.2016.05.070>.
- [12] Yusuf SM, Gao N. Influence of energy density on metallurgy and properties in metal additive manufacturing. *Mater Sci Technol* 2017;33:1269–89. <https://doi.org/10.1080/02670836.2017.1289444>.
- [13] Wu J, Lian K, Deng Y, Jiang P, Zhang C. Multi-objective parameter optimization of fiber laser welding considering energy consumption and Bead geometry. *IEEE Trans Autom Sci Eng* 2022;19:3561–74. <https://doi.org/10.1109/TASE.2021.3126077>.
- [14] Güngör O, Tozlu A, Arslantürk C, Özahi E. District heating based on exhaust gas produced from end-of-life tires in Erzincan: Thermo-economic analysis and optimization. *Energy* 2024;294:130755. <https://doi.org/10.1016/j.energy.2024.130755>.
- [15] Do Carmo PRX, Do Monte JVL, Filho ATDO, Freitas E, Tigre MFFSL, Sadok D, et al. A data-driven model for the optimization of energy consumption of an industrial production boiler in a fiber plant. *Energy* 2023;284:129239. <https://doi.org/10.1016/j.energy.2023.129239>.
- [16] Jeffrey Kuo C-F, Su T-L, Jhang P-R, Huang C-Y, Chiu C-H. Using the Taguchi method and grey relational analysis to optimize the flat-plate collector process with multiple quality characteristics in solar energy collector manufacturing. *Energy* 2011;36:3554–62. <https://doi.org/10.1016/j.energy.2011.03.065>.
- [17] Jinoop AN, Paul CP, Mishra SK, Bindra KS. Laser Additive Manufacturing using directed energy deposition of Inconel-718 wall structures with tailored characteristics. *Vacuum* 2019;166:270–8. <https://doi.org/10.1016/j.vacuum.2019.05.027>.
- [18] DebRoy T, Wei HL, Zuback JS, Mukherjee T, Elmer JW, Milewski JO, et al. Additive manufacturing of metallic components – process, structure and properties. *Prog Mater Sci* 2018;92:112–224. <https://doi.org/10.1016/j.pmatsci.2017.10.001>.
- [19] Ma F, Zhang H, Hon KKB, Gong Q. An optimization approach of selective laser sintering considering energy consumption and material cost. *J Clean Prod* 2018;199:529–37. <https://doi.org/10.1016/j.jclepro.2018.07.185>.
- [20] Peng S, Li T, Zhao J, Lv S, Tan GZ, Dong M, et al. Towards energy and material efficient laser cladding process: modeling and optimization using a hybrid TS-GEP algorithm and the NSGA-II. *J Clean Prod* 2019;227:58–69. <https://doi.org/10.1016/j.jclepro.2019.04.187>.
- [21] Siva Rama Krishna L, Srikanth PJ. Evaluation of environmental impact of additive and subtractive manufacturing processes for sustainable manufacturing. *Mater Today Proc* 2021;45:3054–60. <https://doi.org/10.1016/j.mtproc.2020.12.060>.
- [22] Dong M, Li T, Guo Y, Wu Z, Tang Z, Peng S. Research on modeling and analysis methods of energy consumption of laser cladding systems. *J Dalian Univ Technol* 2018;58:229–37.
- [23] Liu ZY, Li C, Fang XY, Guo YB. Energy consumption in additive manufacturing of metal parts. *Procedia Manuf* 2018;26:834–45. <https://doi.org/10.1016/j.promfg.2018.07.104>.
- [24] Haley JC, Schoenung JM, Lavernia EJ. Modelling particle impact on the melt pool and wettability effects in laser directed energy deposition additive manufacturing. *Mater Sci Eng A* 2019;761:138052. <https://doi.org/10.1016/j.msea.2019.138052>.
- [25] Caiazzo F, Alfieri V, Argenio P, Sergi V. Additive manufacturing by means of laser-aided directed metal deposition of 2024 aluminium powder: investigation and optimization. *Adv Mech Eng* 2017;9. <https://doi.org/10.1177/1687814017714982>.
- [26] Sun J, Zhao Y, Yang L, Zhao X, Qu W, Yu T. Effect of shielding gas flow rate on cladding quality of direct laser fabrication AISI 316L stainless steel. *J Manuf Process* 2019;48:51–65. <https://doi.org/10.1016/j.jmapro.2019.10.011>.
- [27] Sanaei N, Fatemi A, Phan N. Defect characteristics and analysis of their variability in metal L-PBF additive manufacturing. *Mater Des* 2019;182:108091. <https://doi.org/10.1016/j.matdes.2019.108091>.
- [28] Galetto M, Verna E, Genta G. Effect of process parameters on parts quality and process efficiency of fused deposition modeling. *Comput Ind Eng* 2021;156:107238. <https://doi.org/10.1016/j.cie.2021.107238>.
- [29] Li Y, Xiong M, He Y, Xiong J, Tian X, Mativenga P. Multi-objective optimization of laser welding process parameters: the trade-offs between energy consumption and welding quality. *Opt Laser Technol* 2022;149:107861. <https://doi.org/10.1016/j.optlastec.2022.107861>.
- [30] Zhang Z, Liu Z, Wu D. Prediction of melt pool temperature in directed energy deposition using machine learning. *Addit Manuf* 2021;37:101692. <https://doi.org/10.1016/j.addma.2020.101692>.
- [31] Zhu X, Chu J, Wang K, Wu S, Yan W, Chiam K. Prediction of rockhead using a hybrid N-XGBoost machine learning framework. *J Rock Mech Geotech Eng* 2021;13:1231–45. <https://doi.org/10.1016/j.jrmge.2021.06.012>.
- [32] Desale S, Rasool A, Andhale S, Rane P. Heuristic and meta-heuristic algorithms and their relevance to the real World: a Survey. *Int J Comput Eng Res TRENDS* 2015;2.
- [33] Zervoudakis K, Tsafarakis S. A mayfly optimization algorithm. *Comput Ind Eng* 2020;145:106559. <https://doi.org/10.1016/j.cie.2020.106559>.
- [34] Kennedy J, Eberhart R. Particle swarm optimization. *Proc. ICNN95 - Int. Conf. Neural Netw.* 1995;4:1942–8. <https://doi.org/10.1109/ICNN.1995.4489684>.
- [35] Yang X-S, He X. Firefly algorithm: recent advances and applications. *Int J Swarm Intell* 2013;1:36–50. <https://doi.org/10.1504/IJSI.2013.055801>.
- [36] Mehrabian AR, Lucas C. A novel numerical optimization algorithm inspired from weed colonization. *Ecol Inform* 2006;1:355–66. <https://doi.org/10.1016/j.ecoinf.2006.07.003>.
- [37] Chaki S, Bathe RN, Ghosal S, Padmanabham G. Multi-objective optimisation of pulsed Nd:YAG laser cutting process using integrated ANN-NSGAII model. *J Intell Manuf* 2018;29:175–90. <https://doi.org/10.1007/s10845-015-1100-2>.
- [38] Deb K, Pratap A, Agarwal S, Meyarivan T. A fast and elitist multiobjective genetic algorithm: NSGA-II. *IEEE Trans Evol Comput* 2002;6:182–97. <https://doi.org/10.1109/4235.996017>.
- [39] Lundberg SM, Lee S-I. A Unified approach to Interpreting model predictions. *Adv Neural Inf Process Syst* 2017;30. Curran Associates, Inc.
- [40] Liao W, Garg A, Gao L. Design of robust energy consumption model for manufacturing process considering uncertainties. *J Clean Prod* 2018;172:119–32. <https://doi.org/10.1016/j.jclepro.2017.10.155>.
- [41] Ma S, Zhang Y, Lv J, Ge Y, Yang H, Li L. Big data driven predictive production planning for energy-intensive manufacturing industries. *Energy* 2020;211:118320. <https://doi.org/10.1016/j.energy.2020.118320>.
- [42] Wu J, Lin K, Sun J. Pressure or motivation? The effects of low-carbon city pilot policy on China's smart manufacturing. *Comput Ind Eng* 2023;109512. <https://doi.org/10.1016/j.cie.2023.109512>.
- [43] Kumar A. Methods and materials for smart manufacturing: additive manufacturing, Internet of Things, flexible sensors and Soft Robotics. *Ind 4.0 Smart Manuf* 2018;15:122–5. <https://doi.org/10.1016/j.mfglet.2017.12.014>.
- [44] Kellens K, Baumers M, Gutowski TG, Flanagan W, Lifset R, Duflou JR. Environmental dimensions of additive manufacturing: mapping application domains and their environmental implications: environmental dimensions of additive manufacturing. *J Ind Ecol* 2017;21:S49–68. <https://doi.org/10.1111/jiec.12629>.
- [45] Kladovasilakis N, Charalampous P, Kostavelis I, Tzetzis D, Tzovaras D. Impact of metal additive manufacturing parameters on the powder bed fusion and direct

- energy deposition processes: a comprehensive review. *Prog Addit Manuf* 2021;6: 349–65. <https://doi.org/10.1007/s40964-021-00180-8>.
- [46] Qin J, Hu F, Liu Y, Witherell P, Wang CCL, Rosen DW, et al. Research and application of machine learning for additive manufacturing. *Addit Manuf* 2022;52: 102691. <https://doi.org/10.1016/j.addma.2022.102691>.
- [47] Zhu Z, Majewski C. Understanding pore formation and the effect on mechanical properties of High Speed Sintered polyamide-12 parts: a focus on energy input. *Mater Des* 2020;194:108937. <https://doi.org/10.1016/j.matdes.2020.108937>.
- [48] Dzogbewu TC, Amoah N, Fianko SK, Afrifa S, De Beer D. Additive manufacturing towards product production: a bibliometric analysis. *Manuf Rev* 2022;9:1. <https://doi.org/10.1051/mfreview/2021032>.